Biosensors and Bioelectronics 140 (2019) 111345

Contents lists available at ScienceDirect

Biosensors and Bioelectronics

journal homepage: www.elsevier.com/locate/bios

# Multicolor and photothermal dual-readout biosensor for visual detection of prostate specific antigen

Yunyun Wei, Danni Wang, Yingzhi Zhang, Jinhong Sui, Zhangrun Xu*

*Research Center for Analytical Sciences, Northeastern University, Shenyang, 110819, PR China*

ARTICLE INFO

*Keywords:*
Visual detection
Dual-readout sensor
Multicolor immunoassay
Photothermal sensing
Prostate specific antigen

ABSTRACT

Developing a facile and reliable approach for tumor marker detection is crucial in early diagnosis of cancer. Here, a multicolor and photothermal dual signal readout immunosensor was proposed based on a nanoparticle-mediated transformation strategy and used for sensitive detection of prostate specific antigen (PSA). To construct such a platform, $Fe_3O_4$ nanoparticles (NPs) -functionalized graphene oxide was modified with partially complementary DNA and served as the signal probes. In the absence of PSA, the signal probes were captured via hybridization reaction between DNA and PSA aptamer. Subsequently, $Fe_3O_4$ NPs anchored on the probes were transformed into a photothermal agent, Prussian blue NPs, which converted biological signal into heat via the near-infrared laser irradiation, and thus sensitive quantitative detection of PSA was realized by using a thermometer with a lower detection limit of 0.31 ng/mL. Meanwhile, Prussian blue NPs displayed multiply colors by mixing with potassium ferricyanide, and rapid qualitative detection by naked eyes was realized. The two sets of data mutually validate each other, which greatly improved the accuracy and reliability of PSA detection. More strikingly, graphene oxide as the enrichment carrier of $Fe_3O_4$ NPs significantly enhanced the accumulation of Prussian blue NPs in situ, and thus the signal amplification was effectively accomplished. Besides, the sensing strategy avoided the use of enzyme and simplified analysis process. Such a cost-effective and sensitive dual-readout visual protocol opens up new perspectives for personalized diagnosis and on-site detection.

## 1. Introduction

Prostate specific antigen (PSA) is a significant and widely used biomarker of prostate cancer. Developing a facile and accurate approach for tumor marker detection is crucial in clinical early-stage diagnosis and cancer monitoring (Yang and Gao, 2015). Colorimetric immunoassay has attracted intense attention in biological diagnosis, because it does not involve the use of any analytical instruments but human eyes for the readout of biomolecules (Chang et al., 2017; Urbanek et al., 2011; Shah et al., 2013). However, single color changes, from light to dark or from dark to light, result in poor sensitivity for direct readout (Yan et al., 2017). And the intensity change of the same color is susceptible to individual differences, which limits the detection accuracy. To improve the sensitivity and accuracy of naked-eye observation, multicolor strategy was adopted. For example, X. Ma et al. (2017) demonstrated a multicolor sensor by utilizing the oxidation state 3, 3′, 5, 5′-tetramethylbenzidine sulfate (TMB) to etch Au nanoparticles for semi-quantitative detection of biomarkers. Our research group developed a sensitive multicolor visual biosensor based on catalytic hairpin assembly and etching of Au nanorods for telomerase activity detection (Wang et al., 2018). W. Xie et al. (2018) proposed a high-resolution multicolor assay of rabbit immunoglobulin G through the urease-catalyzed urea hydrolysis-induced color change of phenol red. These multicolor sensing strategies show great potential in rapid test with acceptable sensitivity, but they can be only used for qualitative or semi-quantitative analysis. And the analytical results of such single-mode readouts sometimes are influenced by external interferences. To address these issues, great efforts have been made to develop dual-mode detection techniques to provide more comprehensive information. J. Wei et al. developed a photoelectron-chemistry and colorimetry dual-signal immunosensor for microcystin-LR detection (Wei et al., 2018). Wei's group designed a colorimetric and fluorescence detection of cardiac troponin I (Miao et al., 2018). Our research group developed a SERS-fluorescence dual-mode for pH sensing (Yue et al., 2017). Until now, dual-readout visual detection based on multicolor and photothermal strategy has not been reported.

The nanomaterial-mediated photothermal effect has attracted great attention in biomedical field due to the unique light-to-heat conversion property (Yang et al., 2013). The localized heat generated from the photothermal conversion can be accurately and quantitatively

* Corresponding author.
*E-mail address:* xuzr@mail.neu.edu.cn (Z. Xu).

https://doi.org/10.1016/j.bios.2019.111345
Received 24 February 2019; Received in revised form 4 May 2019; Accepted 21 May 2019
Available online 23 May 2019
0956-5663/ 

monitored using a portable thermometer. Prussian blue (PB) as an ancient dye shows a strong optical absorption in the near-infrared (NIR) region, and has been explored as a new generation of NIR laser-driven photothermal agent (Su et al., 2016). Li's group did a good job in nanoparticle-mediated photothermal immunoassay for quantitative detection of prostate-specific antigen (PSA) (Fu et al., 2016). They explored the photothermal effect of iron oxide-mediated TMB-$H_2O_2$ colorimetric system, and applied it for visual quantitative detection of PSA (Fu et al., 2018). However, there are still some challenges in the quantitative detection of biomolecules based on photothermal sensors. On the one hand, the photothermal sensing is easily affected by ambient environment, such as air temperature. To avoid false positive and negative results, it is necessary to combine the photothermal strategy with other detection modes. On the other hand, owing to the high specific surface areas and magnetic property, $Fe_3O_4$ NPs are easily self-agglomerated to reduce their surface energy (Qian et al., 2014; Baghayeri and Veisi, 2015). To address this problem, many materials such as polymers, silicon dioxide, and carbon nanotubes are usually utilized to immobilize the magnetic nanoparticles for keeping their efficiency. Graphene oxide (GO) sheet as an ideal support of various metal nanoparticles is widely applied in biosensors (Cao et al., 2018) owing to its superior properties, such as large surface area and high water solubility (Chen et al., 2012). Loading $Fe_3O_4$ NPs onto graphene oxide could improve the wettability and dispersion of the composite (Sharafeldin et al., 2017). Besides, GO can rapidly bind with single-stranded DNA via the strong π-π stacking interactions between the hexagonal cells of graphene and the ring structure in nucleobases of DNA, and release DNA from its surface with the conformational change of DNA induced by targets (Zhou et al., 2017), avoiding the use of expensive antibody.

Here, we proposed a facile and reliable multicolor and photothermal dual-mode sensor for visual detection of PSA via a simple $Fe_3O_4$-to-PB NP transformation process. Considering the high absorption capacity and water solubility, GO as the enrichment carrier of $Fe_3O_4$ NPs was incorporated to amplify detection signal by in situ increasing the amount of PB NPs. Firstly, GO/$Fe_3O_4$ was fixed on the surface of a microplate via hybridization reaction. When PSA was added, the conformation of PSA aptamer was changed and triggered GO/$Fe_3O_4$ falling off the substrate surface. Subsequently, the remaining $Fe_3O_4$ NPs in the microplate were transformed into PB NPs, which could generate a naked-eye-recognizable multicolor by mixing with potassium ferricyanide. Moreover, PB NPs induced temperature rise of the immunoassay solution via the near-infrared laser irradiation, realizing quantitative readout by using a thermometer. Simultaneous qualitative and quantitative assays were achieved by the combination of multicolor and photothermal detection. Due to different mechanisms and independent signal conversion of the two modes, precise and reliable signal output can be expected.

## 2. Materials and methods

### 2.1. Reagents

Prostate specific antigen was purchased from Linc-Bio Science Co., Ltd. (Shanghai, China). Streptavidin-coated 96-well plates were purchased from Beaver Nano-Technologies Co., Ltd. (Suzhou, China). Graphene oxide was bought from Hangdan Photoelectric Technology Co., Ltd. (Hangzhou, China). Polysorbate 20 was purchased from Alfa Aesar Co., Ltd. (Tianjin, China). Bovine serum albumin (BSA) was purchased from Aladdin Chemistry Co., Ltd. (Shanghai, China). The enzyme-linked immunosorbent assay (ELISA) kit was purchased from Sino Best Biological Technology Co., Ltd (Shanghai, China). Other reagents were purchased from Bodi Chemical Holding Co., Ltd. (Tianjin, China). All reagents were analytical grade unless otherwise stated. Deionized water was used throughout the experiments. DNA oligonucleotides were synthesized by Sangon Biotechnology Co., Ltd. (Shanghai, China). According to the previous report (Yang et al., 2017), we designed the aptamer and the partial complementary DNA (c-DNA), and their sequences are as follows:

PSA-aptamer, 5′-Biotin-ATTAAAGCTCGCCATCAAATAGC-3′;
c-DNA, 5′-$NH_2$-CCCCCCGAGAGCTATTTGATGGCGAG-3′.

### 2.2. Apparatus

The morphological changes were observed employing transmission electron microscopy (TEM, Zeiss, Jena, Thuringia, Germany). Fourier transform infrared (FT-IR) spectroscopy (Nicolet 6700, Thermo Fisher Scientific, Waltham, MA, USA) was employed for the identification of molecular structures. X-Ray diffraction (XRD, PW 3040/60, PANalytical BV, Almelo, Netherland) was applied to investigate the crystallographic structure of products. The Raman spectra were determined by a confocal Raman microscope (XploRA ONE, Horiba Jobin Yvon, France). The UV–vis absorption spectra were recorded by using a microplate reader (BioTek, Synergy H1, USA). The pen-style digital thermometer (model number TP3001, resolution ratio 0.1 °C) with a detection range of −50 to 300 °C was obtained from Zhengzhou Boyang Instrumentation Co., Ltd.

### 2.3. Synthesis of GO/$Fe_3O_4$

GO/$Fe_3O_4$ hybrid material was prepared via a facile solvothermal method according to the previous report (Wu et al., 2013). Ethylene glycol served as both the solvent and the reducing agent in the preparation process. Firstly, 0.40 g GO was added into 60 mL ethylene glycol. The resulting mixture was sonicated until a clear solution was produced. Then 0.65 g $FeCl_3$ as an iron source was added into the solution and further sonicated for 10 min. After 2.60 g sodium acetate was added, the as-prepared solution was stirred vigorously for 20 min. Subsequently, the mixture was transferred to a Teflon-lined stainless steel autoclave and heated at 200 °C for 8 h, and then cooled to room temperature. The black product GO/$Fe_3O_4$ was washed with ethanol for several times, and dried in vacuum.

### 2.4. Synthesis of GO/$Fe_3O_4$-DNA

GO/$Fe_3O_4$ (1.0 mg/mL) was dispersed in phosphate-buffered saline (PBS) buffer (pH = 6.0) and sonicated for 2 h to form a homogenous dispersion. 100 μL freshly prepared coupling agents containing N-ethyl-N'-(3-dimethylaminopropyl) carbodiimide (20 mg/mL) and N-hydroxysuccinimide (10 mg/mL) was added into 900 μL GO/$Fe_3O_4$ to activate the carboxylic acid groups at room temperature for 30 min. The composite was re-dispersed with 800 μL PBS buffer (10 mM, pH = 7.4, containing 137 mM NaCl, 3 mM KCl and 0.05% Polysorbate 20). Then 200 μL of 1.0 μM c-DNA was added to the solutions and shaken at room temperature for 24 h for sufficient immobilization. To remove free unbound DNA, the mixture was collected via a magnetic separation process. The supernatant was discarded, and the sediment was washed three times with PBS buffer. Finally, the composite was re-dispersed with 1 mL PBS (pH = 7.4) and stored at 4 °C for further use.

### 2.5. Procedure of dual-readout colorimetric and photothermal immunoassay

To construct a colorimetric and photothermal dual-mode sensor, 50 μL biotinylated PSA aptamer (1.0 μM) was added to a streptavidin-coated 96-well plate and incubated for 60 min. After washed for three times, the plate was blocked with 200 μL BSA solution (2.0 mg/mL) for 60 min, and then washed thoroughly. The mixture containing 10 μL PSA of different concentrations and 40 μL GO/$Fe_3O_4$-DNA was added to the 96-well plate and incubated for 60 min. After repetitive washing, the unbound GO/$Fe_3O_4$ was removed. To transform $Fe_3O_4$ NPs captured in the immunoassay system into PB NPs, 100 μL HCl (1.0 M) was used to disintegrate $Fe_3O_4$ NPs. Next, 30 μL potassium ferrocyanide ($K_4$[Fe

$(CN)_6$]) solution (90 mM) was added to generate PB NPs based on the reaction between ferric ions and ferrocyanide ions. For multicolor immunoassay, the produced PB NPs dispersion was mixed with 2.5 μL potassium ferricyanide ($K_3[Fe(CN)_6]$) solution (90 mM). The color of the system was recorded by using a digital camera, and the absorbance was measured by using a microplate reader. For photothermal immunoassay, the obtained PB NPs dispersion at different concentrations in the 96-well plate was transferred into 0.2 mL centrifuge tubes. The solutions (100 μL) were irradiated with an 808-nm laser at a power density of 4.67 W·cm$^{-2}$ for 1 min. A portable digital thermometer was immediately inserted (the probe contacting the bottom of the tube) to record the temperature of PB solutions. The highest steady value was recorded as the photothermal measurement signal ($T_1$). The temperature of solution (room temperature) before laser irradiation was used as base temperature ($T_0$). The increase in temperature ($\Delta T$) was the difference value between $T_1$ and $T_0$.

## 3. Results and discussion

### 3.1. Characterization of GO/$Fe_3O_4$ nanocomposites

GO/$Fe_3O_4$ as signal labels played a crucial role in the detection system. The formation of GO/$Fe_3O_4$ was confirmed by FT-IR spectra and X-ray diffraction (XRD). Fig. S1A shows the FT-IR spectra of GO and GO/$Fe_3O_4$ hybrid material. Compared with the spectrum of GO, an apparent band at 594 cm$^{-1}$, which attributes to Fe–O vibrations of $Fe_3O_4$, was observed in the spectrum of the hybrid material. The Raman spectra of GO and GO/$Fe_3O_4$ are presented in Fig. S1B. Similar to GO, GO/$Fe_3O_4$ has two most intense D-band and G-band Raman features ascribing to the feature peaks of graphene materials. But the D/G intensity ratio of the GO/$Fe_3O_4$ is lower than that of GO, indicating that GO in the composite was partially reduced through high-temperature calcination, which facilitated the restoration of $sp^2$ carbon site and enhanced π-π stacking interactions between GO and single strand DNA. XRD was also used to investigate the components of GO/$Fe_3O_4$. As shown in Fig. 1A, a broad peak at 24.5° (002) is derived from GO (Fig. S1C), and the main diffraction peaks at 30.2° (220), 35.6° (311), 43.1° (400), 57.3° (511), 62.8° (440), and 74.8° (533) show the characteristics of $Fe_3O_4$ (JCPDS No. 19–0629) (Qi et al., 2015). These results confirm GO/$Fe_3O_4$ composite was prepared successfully. The morphology of the synthesized GO/$Fe_3O_4$ was imaged by using TEM. Fig. 1C showed that the thin and transparent GO nanosheets resembled silk veil waves and were well loaded with $Fe_3O_4$ NPs. The residual vacancies on the GO surface facilitated spontaneous adsorption of DNA. Besides, the superparamagnetic property of GO/$Fe_3O_4$ was investigated. As shown in the inset of Fig. 1B, the nanocomposites quickly separated from the solution when an external magnetic field was employed, demonstrating that the composites possess excellent magnetism property, and there were enough $Fe_3O_4$ NPs anchored on surface of GO for signal amplification. To further functionalize signal labels, GO/$Fe_3O_4$ was modified by the partial complementary DNA via two interactions: covalent binding between amino groups of DNA and carboxylic groups on the GO, and the strong π-π stacking interactions between the hexagonal cells of GO and ring structures in nucleobases of DNA. The conjugation of DNA with GO/$Fe_3O_4$ was characterized by UV–vis absorption spectroscopy. As shown in Fig. S1D and a weak absorption peak approximately at 260 nm, the ultraviolet absorption maximum of DNA, was observed in the spectrum of the suspension of GO/$Fe_3O_4$-DNA (Wu et al., 2014), demonstrating that c-DNA was successfully modified onto GO/$Fe_3O_4$.

### 3.2. Investigation and confirmation of nanoparticle-mediated transformation process

In this work, a nanoparticle-mediated transformation amplification strategy was introduced to improve sensitivity. Firstly, based on the strong affinity and high specificity between streptavidin (SA) and biotin (Lin et al., 2008), PSA biotin-aptamer was easily fixed on the SA-coated 96-well plate. Each SA could combine with four biotin molecules, which

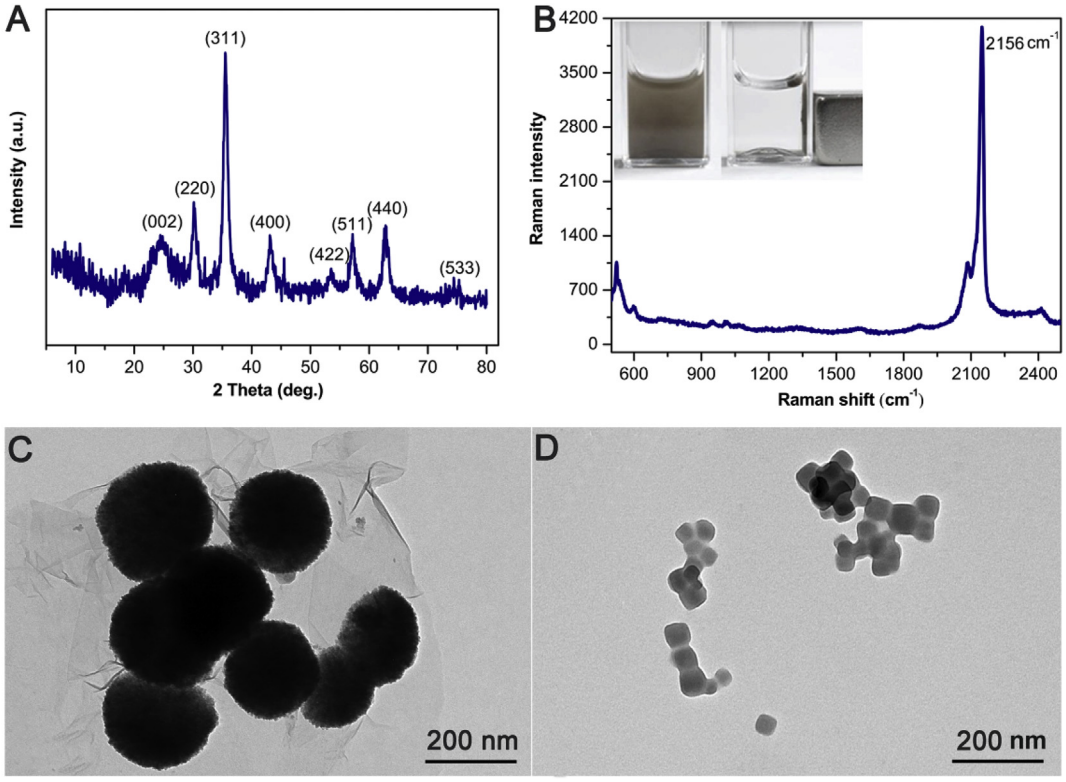


**Fig. 1.** XRD pattern of GO/$Fe_3O_4$ nanocomposites (**A**); Raman spectrum of PB nanoparticles produced in immunoassay (inset is the image of GO/$Fe_3O_4$ hybrid material interacting with an external magnet) (**B**); TEM images of GO/$Fe_3O_4$ hybrid material before (**C**) and after (**D**) transformation.

facilitated the capture of signal probes. Secondly, GO as an effective carrier of $Fe_3O_4$ and c-DNA were used to prepare signal probes. GO/$Fe_3O_4$-DNA was immobilized on the microplate substrate via partial base pairing reaction between c-DNA and aptamer. Meanwhile, some GO/$Fe_3O_4$ bound with the aptamer directly via π-π stacking interactions between the ring structure in nucleobases of the aptamer and hexagonal cells of the GO. Due to the excellent surface area of GO, large amount of $Fe_3O_4$ NPs were fixed in the sensing system along with the GO for magnifying signal. $Fe_3O_4$ NPs anchored on the GO were dissolved in acidic conditions to release $Fe^{3+}$. Subsequently, $Fe^{3+}$ reacted with $K_4[Fe(CN)_6]$ to generate abundant cubic PB NPs with a highly visible blue color. To verify the transformation process from $Fe_3O_4$ NPs to PB NPs, Raman spectroscopy was used to characterize the product. As shown in Fig. 1B, an intense and sharp Raman band at 2156 $cm^{-1}$ was in good agreement with previous reports on the peaks of pure PB NPs (Yin et al., 2017). TEM was applied to describe the morphology changes of nanoparticles before and after conversion. As shown in Fig. 1D, the clear cubic nanoparticles ranging from 30 to 60 nm in side length are displayed, confirming the successful transformation from $Fe_3O_4$ NPs to PB NPs. These results demonstrate the feasibility of colorimetric and photothermal dual-mode strategy based on nanoparticle-mediated transformation.

### 3.3. Mechanism of the dual-readout colorimetric and photothermal immunosensing

To obtain more accurate and reliable results in PSA detection, a novel multicolor and photothermal dual-readout biosensor was fabricated here. The schematic illustration of the dual-signal readout immunosensing is summarized in Scheme 1. Firstly, the signal probe GO/$Fe_3O_4$-DNA was captured onto the 96-well plate. With the addition of PSA, the signal probes would drop off the substrate surface owing to the formation of PSA-aptamer conjugates. The remaining $Fe_3O_4$ NPs in the detection system were transformed into PB NPs under acidic conditions. PB NPs were the core element to realize the temperature and color dual signal readout. For colorimetric detection, PB NPs exhibited a highly visible blue color with a high molar extinction coefficient, which enabled colorimetric sensing. To improve the resolution of visual inspection, a dose-dependent multicolor was generated by adding the color developing agent, $K_3[Fe(CN)_6]$. As shown in Scheme 2, the yellow-colored $K_3[Fe(CN)_6]$ played two roles in the colorimetric detection system. $K_3[Fe(CN)_6]$ reacted with residual $Fe^{2+}$ derived from $Fe_3O_4$ decomposition, produced PB NPs likewise, resulting in more intense color (Karyakin, 2001); $K_3[Fe(CN)_6]$ mixed with blue-colored PB NPs at different ratios to produce multiple vivid colors. As shown in Fig. 2A, $K_4[Fe(CN)_6]$ (a) is colorless and has no absorption within 400–900 nm. PB NPs (b) shows a strong absorption peak at 700 nm. The yellow-colored $K_3[Fe(CN)_6]$ (c) mixing with the PB NPs generated a green-colored solution (d). The absorption peak of the green solution has almost no difference with that of the PB NPs except for a small absorbance peak at 420 nm derived from $K_3[Fe(CN)_6]$. These results proved no new substance was produced. The intensity of the absorbance, especially at 700 nm, increased slightly, demonstrating the formation of new PB NPs derived from the reaction between $Fe^{2+}$ and $K_3[Fe(CN)_6]$. More interesting, as revealed in Fig. 2B, the introduction of $K_3[Fe(CN)_6]$ at different doses into the same PB solution produced four colors without an apparent change of intensity at the maximum absorption, illustrating that $K_3[Fe(CN)_6]$ played the main role in multicolor generation.

To achieve the best dose-dependent color conversion, we optimized the dose of $K_3[Fe(CN)_6]$. The final color of the solution in each well is shown in Fig. 3A. As the volume of $K_3[Fe(CN)_6]$ (90 mM) changed from 0 to 10.0 μL, the solution color with the same content of GO/$Fe_3O_4$ changed from blue to green and gradually deepened. With the amount of GO/$Fe_3O_4$ composites increasing from 2.0 to 64 μg (calculated by volume), the color changes (from yellow to yellow-green, green, green-blue, and finally blue) were observed and easily distinguished by naked eyes. When the volume of the added $K_3[Fe(CN)_6]$ was 2.5 μL, the resulted solutions showed an obvious color gradient (yellow, green, and blue), which corresponded well with the analyte concentration gradient (from low to high). Therefore, 2.5 μL $K_3[Fe(CN)_6]$ was considered as the optimal dose and utilized in the following experiments. The UV–vis spectra of the solutions containing 2.5 μL $K_3[Fe(CN)_6]$ and different doses of GO/$Fe_3O_4$ were recorded from 350 nm to 900 nm in Fig. 3B. An apparent increase of absorbance at 700 nm was presented as the content of GO/$Fe_3O_4$ increased. According to the absorption curve (Fig. S2), the limit of detection (LOD) was calculated as low as 0.15 μg, proving that the development of a sensitive multicolor immunoassay, based on nanoparticle-mediated transformation process, is feasible.

For photothermal detection, the light-heat conversion reagents

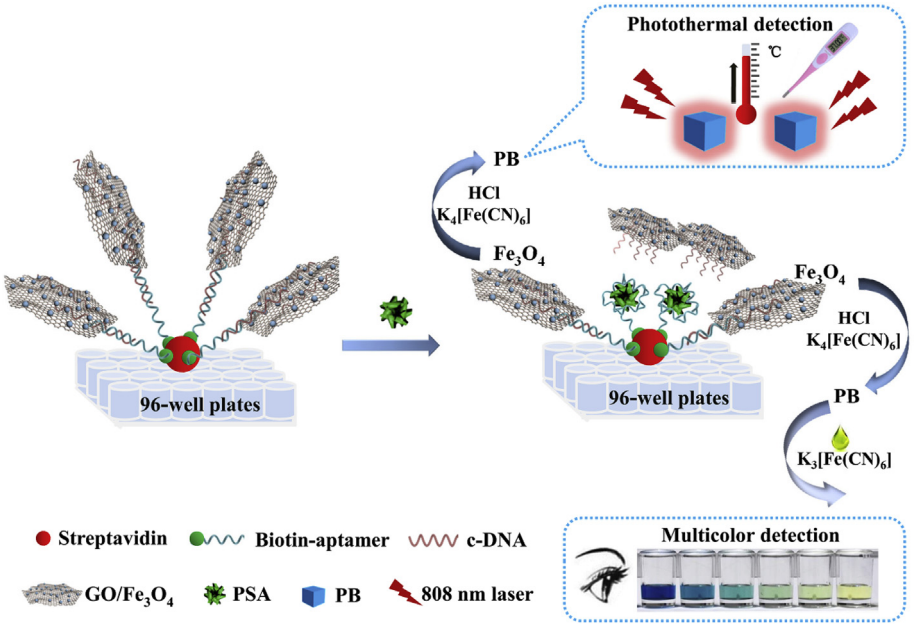


**Scheme 1.** Schematic diagrams of multicolor and photothermal dual-readout visual sensing platform.

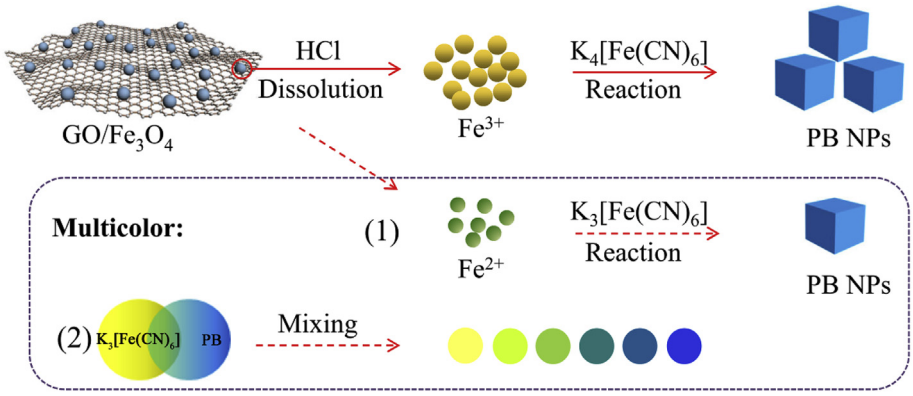


**Scheme 2.** Schematic illustration of the $Fe_3O_4$-to-PB NP conversion process and the mechanism of multicolor generation.

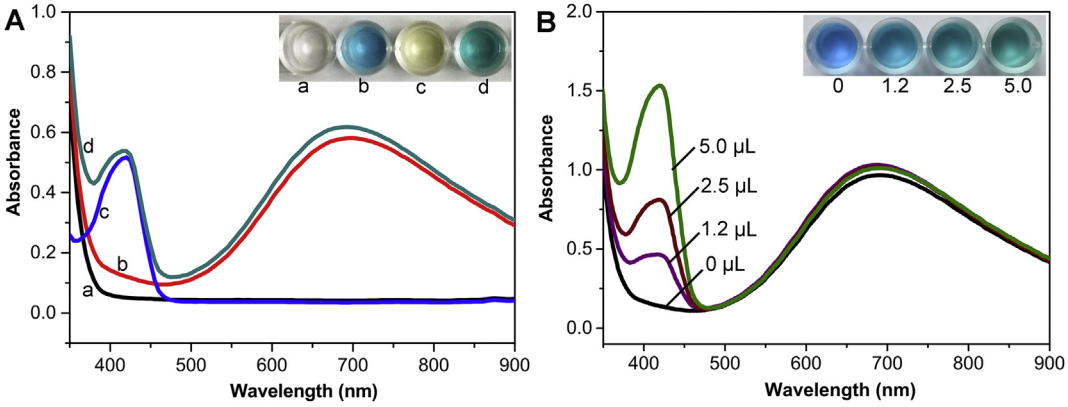


**Fig. 2.** (**A**) Photographs and UV–vis absorption spectra of (a) $K_4[Fe(CN)_6]$, (b) PB NPs, (c) $K_3[Fe(CN)_6]$ and (d) mixture of $K_3[Fe(CN)_6]$ and PB NPs. (**B**) Photographs and UV–vis absorption spectra of PB solutions after adding different doses of $K_3[Fe(CN)_6]$ (0, 1.2, 2.5, and 5.0 μL).

usually have strong optical absorption in the NIR region. As shown in Fig. 2A, PB NPs displayed a broad absorption band from 500 nm to 900 nm with a strong absorption peak at 700 nm, which stems from the charge transfer between Fe (II) and Fe (III), providing the possibilities for photothermal detection. To explore the photothermal effect of PB NPs, 1.0 mL PB NPs aqueous dispersion at different concentrations were irradiated with 808 nm laser at a power density of 2.73 $W{\cdot}cm^{-2}$ for 10 min. A portable digital thermometer was inserted to monitor the temperature variation, and the temperature was recorded every 10 s during the irradiation. Using water as control, the value of temperature increase ($\Delta T$) gradually increased with the concentrations of PB NPs changing from 0.0125 to 0.0375 mg/mL, as shown in Fig. 4A. Even with PB NPs at a low concentration of 0.0125 mg/mL, it also caused a temperature increase of 17.2 °C. Besides, irradiation for only 1 min at a power density of 2.73 $W{\cdot}cm^{-2}$ can result in a rapid temperature increase of 21.2 °C at 0.0375 mg $mL^{-1}$. These results demonstrate the feasibility of using PB NPs for the photothermal immunoassay.

To evaluate the photothermal effect before and after the $Fe_3O_4$-to-PB NPs transformation, comparison of the temperature increases ($\Delta T$) between $GO/Fe_3O_4$ and PB NPs is shown in Fig. 4B. Their aqueous

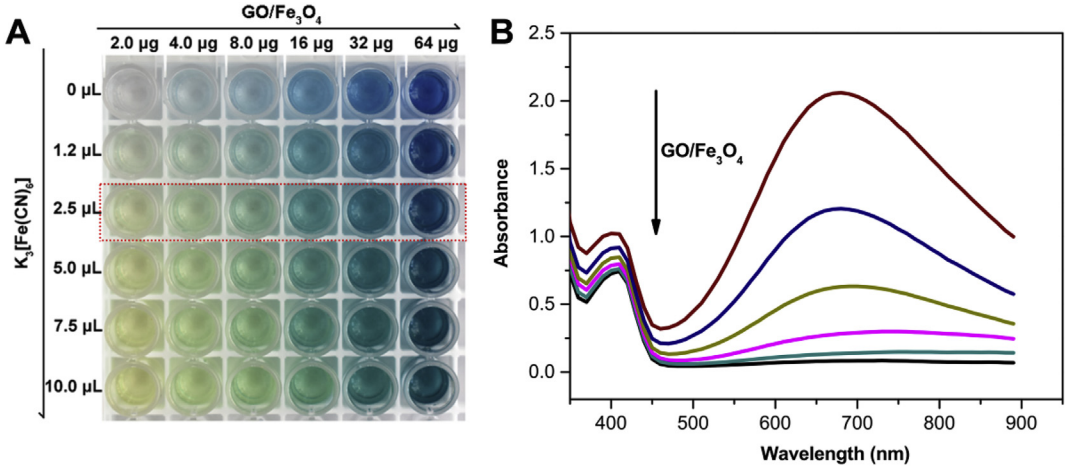


**Fig. 3.** (**A**) Photographs of multicolor solutions with different doses of $GO/Fe_3O_4$ and $K_3[Fe(CN)_6]$. (**B**) UV–vis spectra of colorimetric reaction solutions with different doses of $GO/Fe_3O_4$ when the volume of the added $K_3[Fe(CN)_6]$ was 2.5 μL.

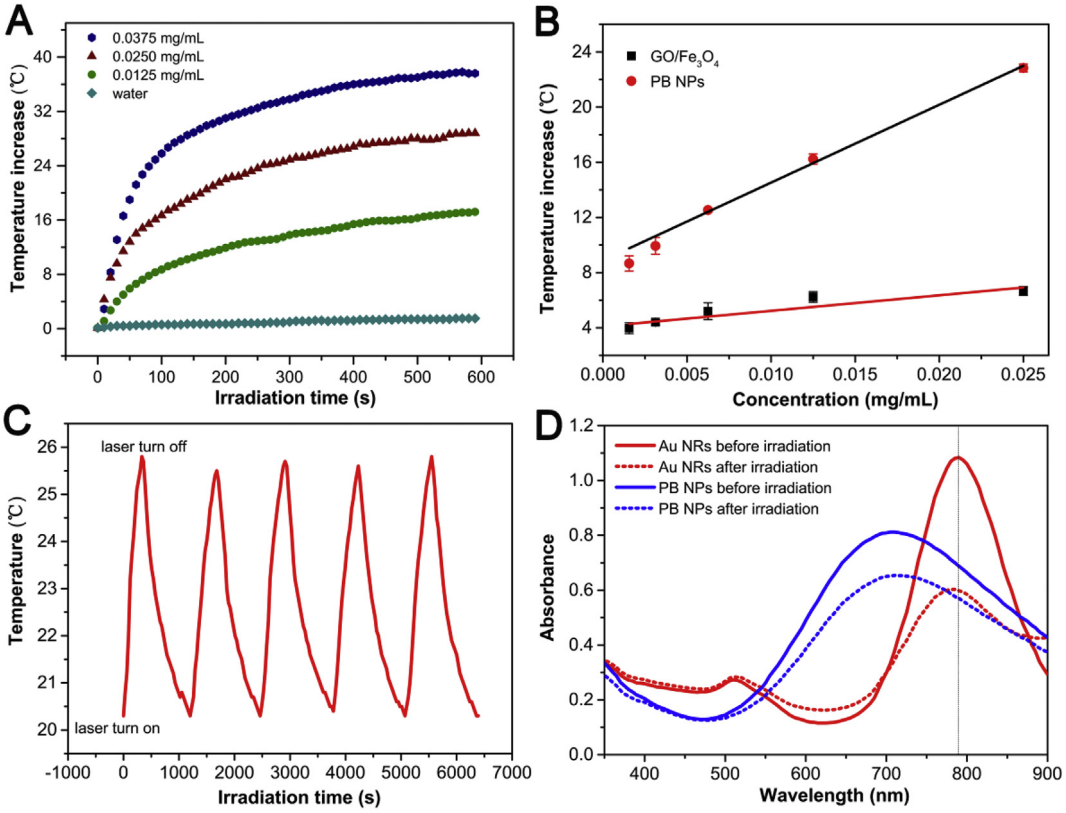


**Fig. 4.** (**A**) Comparison of temperature increase of water and PB NPs at different concentrations during the irradiation with a power density of 2.73 W $cm^{-2}$ for 10 min. (**B**) Comparison of temperature increase between $GO/Fe_3O_4$ and PB NPs at different concentrations after the irradiation with a power density of 4.67 W $cm^{-2}$ for 1 min. (**C**) Temperature variation of PB NPs aqueous dispersion via on/off laser irradiation for five cycles at a power density of 2.73 W·$cm^{-2}$. (**D**) UV–vis spectra of PB NPs and Au NRs aqueous dispersions before and after irradiation with a power density of 4.67 W $cm^{-2}$ for 3 min.

dispersions (100 μL) were exposed to the laser at a power density of 4.67 W·$cm^{-2}$ for 1 min. As the concentration increased, the temperature of PB NPs increased dramatically by 22.8 °C at the concentration of 0.0250 mg/mL. By comparison, the temperature elevation of $GO/Fe_3O_4$ NPs changed slowly after $GO/Fe_3O_4$ NPs were irradiated at the same conditions. Even at the concentration of 0.0250 mg/mL, it only rose by 6.7°C, much lower than that of PB NPs. These detailed studies indicate the excellent photothermal effect of PB NPs. Furthermore, the temperature increase was proportional to the concentration of PB NPs and showed a linear relationship with the square of correlation coefficient of 0.9922, which demonstrates the feasibility of the photothermal strategy for quantitative analysis of biomolecules.

To measure the photothermal stability, the temperature variation of PB aqueous dispersion during five cycles of on/off irradiation was monitored. Firstly, PB NPs aqueous dispersion (0.01 mg/mL) was irradiated with an 808 nm laser at a power density of 2.73 W·$cm^{-2}$ for 6 min, and then the dispersion was cooled naturally to room temperature. Subsequently, another irradiation cycle was carried out. As shown in Fig. 4C, PB NPs aqueous dispersion displays a stable temperature variation during five irradiation cycles, which implies good photothermal stability of PB NPs. UV–vis spectra was employed to further investigate the photostability of PB NPs. Au nanorods (NRs) were chosen as a control photothermal reagent, which were prepared by using a seed-mediated growth method (Huang et al., 2006). The dispersions of Au NRs and PB NPs were continuously exposed to an 808 nm laser at a power density of 4.67 W·$cm^{-2}$ for 3 min. Au NRs show obvious change in absorption spectrum after the irradiation (Fig. 4D). The height of the maximum absorption peak at 790 nm decreased dramatically, and the peak exhibited 10-nm blue shift. The relatively poor photostability was caused by the photo-induced melt of Au NRs after laser irradiation (Link et al., 1999; Ungureanu et al., 2011). Reversely, owing to the high structural stability of PB NPs (Fu et al., 2014), only minor change in UV–vis absorption spectra of their dispersions was observed without any peak shift, demonstrating the good photostability of PB NPs. The good photothermal properties allow the reuse of PB NPs in photothermal sensing.

### 3.4. Performance of the dual-readout colorimetric and photothermal detection of PSA

With 2.5 μL of $K_3[Fe(CN)_6]$ used for multicolor generation, PSA with concentration ranging from 1 ng/mL to 128 ng/mL was tested by the established dual-signal readout biosensor. Fig. 5A displays the side view photographs of immunoassay solutions in the 96-well plate. From left to right, the solution gradually turned from blue to colorless with the increase of PSA concentration. After adding $K_3[Fe(CN)_6]$, a vivid multicolor changing from blue-green to green, yellow-green, and yellow was obtained, as shown in Fig. 5B. Compared with the single color, the multiple colors were easily differentiated from each other by naked eyes. Fig. 5C and Fig. 5D describe the corresponding UV–vis absorption spectra of the single and the multicolor immunoassay solutions from 400 nm to 900 nm, respectively. The intensity of the UV–vis absorption peak at 700 nm gradually decreased as the PSA concentration increased. It is worth noting that the introduction of $K_3[Fe(CN)_6]$ produced new PB NPs, resulting in more intense color and the slight increase of absorbance. And there is a well linear relationship between the absorbance at 700 nm ($A$) and the logarithm of PSA concentration (Log $C_{PSA}$) in the multicolor system (Fig. 5F), with the square of the correlation coefficient of 0.9891 ($A$ = 0.7073–0.2673 Log $C_{PSA}$). Although the color change can be used for rapid qualitative or semi-quantitative analysis by naked eyes, an UV–vis absorption spectrometer is usually required to accurately quantify the PSA concentrations.

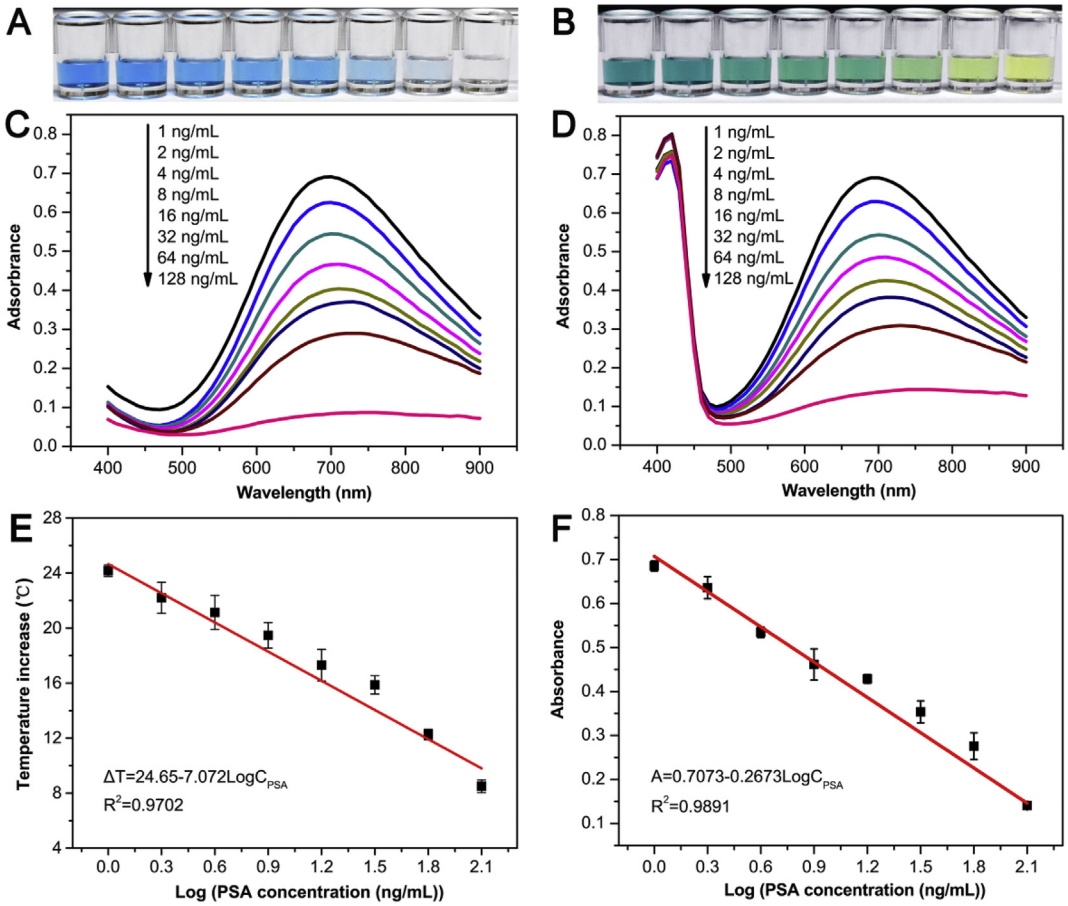


**Fig. 5.** Side view photographs of the single color (**A**) and multicolor (**B**) immunoassay solutions for PSA detection at different concentrations; The corresponding UV–vis absorption spectra of the single color (**C**) and multicolor (**D**) immunoassay solutions; Calibration plots of the temperature increase vs the logarithm of PSA concentration (**E**) (The immunoassay solutions were irradiated by the 808 nm laser for 1 min at a power density of 4.67 $W{\cdot}cm^{-2}$); Calibration plots of the multicolor absorbance at 700 nm vs the logarithm of PSA concentration (**F**). (For interpretation of the references to color in this figure legend, the reader is referred to the Web version of this article.)

To address the above problem, a complementary quantitative detection strategy was performed by using a portable thermometer. Fig. 5E displays the temperature variation of immunoassay solutions with different concentrations of PSA. The $\Delta T$ is linearly correlated with the logarithm of PSA concentrations with a reliable correlation coefficient of 0.9702 ($\Delta T$ = 24.65–7.072 Log $C_{PSA}$) when the PSA concentration ranging from 1 to 128 ng/mL. According to the rule of three times standard deviation of background divided by the slope of the standard curve, the LOD was calculated to be as low as 0.31 ng/mL. The threshold concentration of PSA in clinical prostate cancer diagnosis is 4.0 $ng{\cdot}mL^{-1}$, reported in the previous works (Tang et al., 2017; Yang et al., 2017). Therefore, the sensitivity of the new photothermal detection platform can meet the demand of prostate cancer diagnosis in practical clinical detection. Besides, compared with other common detection methods for PSA (Table S1), this nanoparticle-mediated quantitative method by using a thermometer displayed an expected sensitivity. Meanwhile, it was more cost-effective than other methods without using enzyme, antibody and noble metal.

To investigate the specificity of the dual-signal readout immunoassay sensor, several common interfering biomolecules in serum, such as bovine serum albumin (BSA, 60 μg/mL), hemoglobin (HGB, 60 μg/mL), vascular endothelial growth factor (VEGF, 160 ng/mL) and carcinoembryonic antigen (CEA, 160 ng/mL) were measured. As shown in Fig. 6A, no apparent temperature and absorbance changes were observed for the interfering substances while a dramatic decline for the target PSA (16 ng/mL). These results demonstrate the high specificity of dual-readout visual detection of PSA. Besides, stability is another important criterion for the evaluation of detection methods in practical application. The nanoparticle-mediated multicolor immunoassay usually exhibits significantly enhanced stability. To verify this characteristic, using PSA (64 ng/mL) as a model analyte, we recorded the absorbance changes of immunoassay solution which was exposed to air at room temperature for 160 min, as shown in Fig. 6B. No remarkable change of the absorbance at 700 nm was observed within nearly 3 h, demonstrating the good stability of the developed multicolor assay. Likewise, the temperature of immunoassay solution kept almost invariable during the successive on/off cycle irradiation for 160 min. These results imply good photothermal stability of PB NPs, which allows re-measurement in practical applications. It is worth noting that PB NPs is unstable in strong alkaline solution, so the immunoassay solution cannot contact with strong alkali materials. In our work, PB NPs were derived from the decomposition of $Fe_3O_4$ NPs in HCl solution, and thus presented a high stability.

To estimate the accuracy of the established analytical method, a standard addition method was employed for real sample analysis. The serum samples from normal human were pre-diluted 10 folds using PBS and spiked with different concentrations of PSA for photothermal and absorbance determination, respectively. The commercial ELISA kit as a reference was used to quantify the concentration of PSA in serum according to the manufacturer's instructions. As shown in Table S2, the recovery rates of the spiked PSA samples in the photothermal assay were 106% and 103%, and in the absorbance determination were 113% and 104%. Similar to the ELISA kits (111% and 95.6%), these recoveries were within the acceptable criteria for bioanalytical method

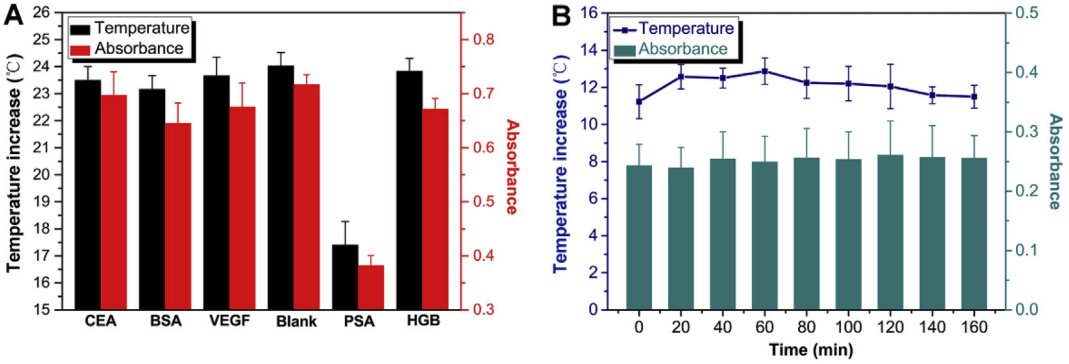


**Fig. 6.** (**A**) Specificity of the dual-signal readout biosensor towards different targets. The concentrations of BSA and HGB were 60 μg/mL, CEA and VEGF were 160 ng/mL, and PSA was 16 ng/mL, respectively. (**B**) Stability evaluation of the dual-signal readout biosensor in the presence of PSA at 64 ng/mL. The immunoassay solutions were irradiated by the 808 nm laser for 1 min at a power density of 4.67 $W \cdot cm^{-2}$.

validation. The commercial ELISA kit has the advantages of high specificity, simplicity, and intuitive detection, but the quantitative detection often relies on optical measurements such as ultraviolet absorption detection. And the sensitivity and accuracy of the testing results are limited due to the vulnerable enzymes used for signal amplification (*Hu et al. 2015*). In our work, the dual-mode strategy on the basis of the multicolor and temperature variation provided more comprehensive information of biomarkers. Two sets of data can mutually validate each other, and false positive and false negative detection can be avoided. Significantly, the thermometer-based quantitative detection is low-cost, portable and widely-available. The analysis process was simplified greatly without using any specialized software for equipment control and data processing. Besides, the introduction of nanoparticle-mediated conversion strategy avoided the use of enzyme, improving the accuracy and reliability of detection results. Therefore, the proposed immunoassay has a broad application potential in real sample analysis.

## 4. Conclusions

In conclusion, we constructed a multicolor and temperature-based dual-signal readout strategy for low-cost, intuitive and reliable detection of PSA. The method has a low LOD and a wide linear range, which are comparable to or even better than those of other single mode assays. Such favorable properties are ascribed to the following reasons: (1) GO as the carrier of $Fe_3O_4$ increased the production of PB NPs in situ for magnifying signals. (2) The transformation product, PB NPs, exhibited good photothermal efficiency and produced multiply vivid color, realizing temperature and color dual signal readout. (3) Two sensing modes mutually validated each other, a more precise and reliable result can be obtained. Both colorimetric and photothermal sensing showed a high stability, allowing re-measurement in practical applications. In addition, the introduction of nanoparticle-mediated conversion strategy avoided the use of enzyme and noble metal catalyst, and simplified biological analysis process. The light source that we used here is still relatively expensive. However, with the rapid development of photoelectric devices, more and more hand-held NIR laser pointers are becoming commercially available and affordable to a physician's office or individuals. Accordingly, the designed dual-mode immunoassay not only provides a powerful platform for visual detection of tumor markers, but also provides new opportunities for personally affordable bioassays in low-resource setting.

## CRediT authorship contribution statement

**Yunyun Wei:** Conceptualization, Data curation, Investigation, Writing - original draft, Validation. **Danni Wang:** Conceptualization, Funding acquisition, Investigation, Methodology. **Yingzhi Zhang:** Software, Data curation, Validation, Writing - review & editing. **Jinhong Sui:** Data curation, Validation, Methodology, Writing - review & editing. **Zhangrun Xu:** Funding acquisition, Project administration, Resources, Supervision, Writing - review & editing.

## Acknowledgements

This work was supported by the National Natural Science Foundation of China (21874015 and 21675020).

## Appendix A. Supplementary data

Supplementary data to this article can be found online at https://doi.org/10.1016/j.bios.2019.111345.

## References

Baghayeri, M., Veisi, H., 2015. Biosens. Bioelectron. 74, 190–198.
Cao, J.T., Yang, J.J., Zhao, L.Z., Wang, Y.L., Wang, H., Liu, Y.M., Ma, S.H., 2018. Biosens. Bioelectron. 99, 92–98.
Chang, C.C., Wang, G., Takarada, T., Maeda, M., 2017. ACS Appl. Mater. Interfaces 9 (39), 34518–34525.
Chen, D., Feng, H., Li, J., 2012. Chem. Rev. 112 (11), 6027–6053.
Fu, G., Sanjay, S.T., Dou, M., Li, X., 2016. Nanoscale 8 (10), 5422–5427.
Fu, G., Sanjay, S.T., Zhou, W., Brekken, R.A., Kirken, R.A., Li, X., 2018. Anal. Chem. 90 (9), 5930–5937.
Fu, G., Liu, W., Li, Y., Jin, Y., Jiang, L., Liang, X., Dai, Z., 2014. Bioconjug. Chem. 25 (9), 1655–1663.
Huang, X.H., El-Sayed, I.H., Qian, W., El-Sayed, M.A., 2006. J. Am. Chem. Soc. 128, 2115.
Hu, R., Liu, T., Zhang, X.B., Yang, Y., Chen, T., Wu, C., Liu, Y., Zhun, G., Huan, S., Fu, T., Tan, W., 2015. Anal. Chem. 87 (15), 7746–7753.
Karyakin, A.A., 2001. Electroanalysis 13, 813–819.
Lin, Z., Wang, X., Li, Z.J., Ren, S.Q., Chen, G.N., Ying, X.T., Lin, J.M., 2008. Talanta 75 (4), 965–972.
Link, S., Burda, C., Mohamed, M.B., Nikoobakht, B., El-Sayed, M.A., 1999. J. Phys. Chem. A 103, 1165.
Ma, X., Lin, Y., Guo, L., Qiu, B., Chen, G., Yang, H.H., Lin, Z., 2017. Biosens. Bioelectron. 87, 122–128.
Miao, L., Zhu, C., Jiao, L., Li, H., Du, D., Lin, Y., Wei, Q., 2018. Anal. Chem. 90 (3), 1976–1982.
Qian, J., Yang, X., Jiang, L., Zhu, C., Mao, H., Wang, K., 2014. Sensor. Actuator. B Chem. 201, 160–166.
Qi, T., Huang, C., Yan, S., Li, X.J., Pan, S.Y., 2015. Talanta 144, 1116–1124.
Shah, P., Zhu, X., Li, C.Z., 2013. Expert Rev. Mol. Diagn. 13 (1), 83–91.
Su, Y., Teng, Z., Yao, H., Wang, S., Tian, Y., Zhang, Y., Liu, W., Tian, W., Zheng, L., Lu, N., Ni, Q., Su, X., Tang, Y., Sun, J., Liu, Y., Wu, J., Yang, G., Lu, G., Zhang, L., 2016. ACS Appl. Mater. Interfaces 8, 17038–17046.
Sharafeldin, M., Bishop, G.W., Bhakta, S., El-Sawy, A., Suib, S.L., Rusling, J.F., 2017. Biosens. Bioelectron. 91, 359–366.
Tang, Z., Wang, L., Ma, Z., 2017. Biosens. Bioelectron. 92, 577–582.
Ungureanu, C., Kroes, R., Petersen, W., Groothuis, T.A., Ungureanu, F., Janssen, H., van Leeuwen, F.W., Kooyman, R.P., Manohar, Svan, Leeuwen, T.G., 2011. Nano Lett. 11, 1887–1894.
Urbanek, C., Goodison, S., Chang, M., Porvasnik, S., Sakamoto, N., Li, C.Z., Boehlein, S.K., Rosser, C.J., 2011. BMC Canc. 11 (1), 233.
Wang, D., Guo, R., Wei, Y., Zhang, Y., Zhao, X., Xu, Z., 2018. Biosens. Bioelectron. 122, 247–253.
Wei, J., Chang, W., Qileng, A., Liu, W., Zhang, Y., Rong, S., Lei, H., Liu, Y., 2018. Anal. Chem. 90 (15), 9606–9613.

Wu, Q., Feng, C., Wang, C., Wang, Z., 2013. Colloids Surfaces B Biointerfaces 101, 210–214.
Wu, S., Duan, N., Shi, Z., Fang, C., Wang, Z., 2014. Anal. Chem. 86 (6), 3100–3107.
Xie, W., Lei, L., Tian, M., Zhang, Z., Liu, Y., 2018. Analyst 143, 2901–2907.
Yan, X., Li, H., Hu, T., Su, X., 2017. Biosens. Bioelectron. 91, 232–237.
Yang, X., Gao, Z., 2015. Chem. Commun. 51, 6928–6931.
Yang, J., Shen, D., Zhou, L., Li, W., Li, X., Yao, C., Wang, R., El-Toni, A.M., Zhang, F., Zhao, D., 2013. Chem. Mater. 25 (15), 3030–3037.
Yang, K., Hu, Y., Dong, N., Zhu, G., Zhu, T., Jiang, N., 2017. Biosens. Bioelectron. 94, 286–291.
Yin, Y., Li, Q., Ma, S., Liu, H., Dong, B., Yang, J., Liu, D., 2017. Anal. Chem. 89 (3), 1551–1557.
Yue, S., Sun, X., Wang, N., Wang, Y., Wang, Y., Xu, Z., Chen, M., Wang, J., 2017. ACS Appl. Mater. Interfaces 9 (45), 39699–39707.
Zhou, Z., Hao, N., Zhang, Y., Hua, R., Qian, J., Liu, Q., Li, H., Zhu, W., Wang, K., 2017. Chem. Commun. 53 (52), 7096–7099.